arXiv:1606.05595v1 [cond-mat.stat-mech] 17 Jun 2016

# Structure and dynamics of binary liquid mixtures near their continuous demixing transitions

Sutapa Roy,[1,*] S. Dietrich,[1] and Felix Höfling[1,2]

[1]*Max-Planck-Institut für Intelligente Systeme, Heisenbergstr. 3, 70569 Stuttgart, Germany, and IV. Institut für Theoretische Physik, Universität Stuttgart, Pfaffenwaldring 57, 70569 Stuttgart, Germany*
[2]*Fachbereich Mathematik und Informatik, Freie Universität Berlin, Arnimallee 6, 14195 Berlin, Germany*

(Dated: June 20, 2016)

The dynamic and static critical behavior of five binary Lennard-Jones liquid mixtures, close to their continuous demixing points (belonging to the so-called model $H'$ dynamic universality class), are studied computationally by combining semi-grand canonical Monte Carlo simulations and large-scale molecular dynamics (MD) simulations, accelerated by graphic processing units (GPU). The symmetric binary liquid mixtures considered cover a variety of densities, a wide range of compressibilities, and various interactions between the unlike particles. The static quantities studied here encompass the bulk phase diagram (including both the binodal and the $\lambda$-line), the correlation length, the concentration susceptibility, the compressibility of the finite-sized systems at the bulk critical temperature $T_c$, and the pressure. Concerning the collective transport properties, we focus on the Onsager coefficient and the shear viscosity. The critical power-law singularities of these quantities are analyzed in the mixed phase (above $T_c$) and non-universal critical amplitudes are extracted. Two universal amplitude ratios are calculated. The first one involves static amplitudes only and agrees well with the expectations for the three-dimensional Ising universality class. The second ratio includes also dynamic critical amplitudes and is related to the Einstein–Kawasaki relation for the interdiffusion constant. Precise estimates of this amplitude ratio are difficult to obtain from MD simulations, but within the error bars our results are compatible with theoretical predictions and experimental values for model $H'$. Evidence is reported for an inverse proportionality of the pressure and the isothermal compressibility at the demixing transition, upon varying either the number density or the repulsion strength between unlike particles.

PACS numbers: 64.60.Ht, 64.70.Ja, 66.10.cg
Keywords: critical phenomena, transport properties of fluids, Monte Carlo simulations, and molecular dynamics

## I. INTRODUCTION

Upon approaching continuous phase transitions at $T_c$, the order parameter fluctuations with long wavelengths become prevalent [1, 2]. This is accompanied by the unlimited increase of the bulk correlation length $\xi(\tau \to 0^{\pm}) \simeq \xi_0^{\pm}|\tau|^{-\nu}$, where $\tau = (T - T_c)/T_c$ is the reduced temperature and $\nu$ is one of the standard bulk critical exponents. The coefficients $\xi_0^{\pm}$ are *per se* non-universal amplitudes but they form a universal ratio $\xi_0^+/\xi_0^-$. This divergence of $\xi$ leads to singularities in and scaling behavior of various thermodynamic and transport properties, commonly known as critical phenomena [1–6]. Close to $T_c$ and in line with renormalization group theory [7] the corresponding critical exponents and scaling functions turn out to be universal, i.e., they depend only on gross features such as the spatial dimension $d$, the symmetry of the order parameter, the range of interactions, and hydrodynamic conservation laws, forming universality classes. Binary liquid mixtures, exhibiting second order demixing transitions, serve as experimentally particularly suitable representatives of the corresponding Ising universality class (see, e.g., Refs. [5, 8, 9]). Besides probing critical phenomena as such, recently these critical demixing transitions in confined binary liquid mixtures have gained significant renewed attention in the context of critical Casimir forces [10] and of non-equilibrium active Brownian motion of colloidal particles, driven by diffusiophoresis in binary liquid solvents [11].

Static critical phenomena in binary liquid mixtures are rather well understood and reported in the literature, encompassing theory [1–5], experiments (see, e.g., Refs. [8, 9, 12]), and computer simulations (see, e.g., Refs. [13–16]). Comparatively, much less is known about their dynamic properties. In particular, simulation studies of dynamic critical phenomena are very recent and scarce. So far, most of the computational studies of critical transport properties in binary liquid mixtures have been focused on a specific and single, highly incompressible fluid. However, probing the concept of universality and its onset for these kind of systems requires simulations of various distinct binary liquid mixtures. In order to alleviate this dearth, we have performed MD simulations concerning the universal critical behavior [3–6] of several static and dynamic quantities, for five symmetric binary liquid mixtures. The fluids considered here exhibit distinct number densities $\varrho$ and compressibilities and cover a broad range of critical temperatures. Inter alia, this allows us to investigate the density dependence of certain critical amplitudes which together with critical exponents determine the qualitative importance of the corresponding critical singularities. In this respect our study is supposed to shed light on apparently contradictory theoretical predictions [17, 18] concerning critical amplitude ratios, for which there is also a lack of experimental data. Besides the interest in them in its own right, they play also an important role for the dynamics of critical Casimir forces [19], the understanding of which is still in an early stage. The compilation of non-universal critical amplitudes, which has been obtained from our study, will also be beneficial for future simulation studies involving the demixing of binary liquids, for which one can then select the most appropriate fluid model. The MD simulations are carried out in

* sutapa@is.mpg.de

the mixed phase, i.e., approaching $T_c$ from above (for an upper critical demixing point); to the best of our knowledge, there are no computational investigations of the critical transport in binary liquid mixtures approaching $T_c$ from below. In addition we have estimated certain universal relations [3, 4] involving various critical amplitudes above $T_c$.

The crucial feature of the static critical phenomena is the unlimited increase of the aforementioned correlation length $\xi$, which is a measure of the spatial extent of a typical order parameter fluctuation. In a binary liquid mixture, for a demixing transition the order parameter is the deviation of the local concentration from its critical value whereas for a liquid–vapor transition the order parameter is the deviation of the local number density from its critical value. The static critical singularities obey power laws:

$$\begin{gathered}\varphi(\tau \to 0^-) \simeq \varphi_0 |\tau|^\beta, \quad \xi \simeq \xi_0^\pm |\tau|^{-\nu}, \\ \chi \simeq \chi_0^\pm |\tau|^{-\gamma}, \quad C_V \simeq A^\pm |\tau|^{-\alpha},\end{gathered} \tag{1}$$

where $\varphi$, $\chi$, and $C_V$ are the order parameter, the susceptibility, and the specific heat at constant volume, respectively. Any two of these static critical exponents are independent; all remaining ones follow from scaling relations [2] such as

$$\alpha + 2\beta + \gamma = 2, \qquad \nu d = 2 - \alpha, \tag{2}$$

where $d$ is the spatial dimension. Unlike the critical exponents, the critical amplitudes depend on whether $T_c$ is approached from above or from below. For the Ising universality class in $d = 3$, the exponents are known to high accuracy [5]:

$$\alpha \approx 0.110,\ \beta \approx 0.325,\ \gamma \approx 1.239,\ \text{and}\ \ \nu \approx 0.630. \tag{3}$$

The critical amplitudes, both above and below $T_c$, are non-universal. However, certain ratios of the critical amplitudes, such as $\xi_0^+/\xi_0^-$ and $\chi_0^+/\chi_0^-$, are known to be universal [4, 12]; for the Ising universality class in $d = 3$ one has

$$\xi_0^+/\xi_0^- \approx 2.02 \text{ and } \chi_0^+/\chi_0^- \approx 4.9. \tag{4}$$

Dynamic critical phenomena are governed by the relaxation time $t_r$ which diverges upon approaching $T_c$ as

$$t_r \sim \xi^z, \tag{5}$$

leading to critical slowing down [3]. This entails thermal singularities in various collective transport coefficients, e.g., the mutual diffusivity $D_\mathrm{m}$ and the shear viscosity $\bar{\eta}$ [6]:

$$D_\mathrm{m} \sim \xi^{-x_D} \quad \text{and} \quad \bar{\eta} \sim \xi^{x_\eta}. \tag{6}$$

The dynamic critical exponents $z$, $x_D$, and $x_\eta$ satisfy scaling relations as well [3, 6],

$$x_D = d - 2 + x_\eta \quad \text{and} \quad z = d + x_\eta\,, \tag{7}$$

leaving scope for only one independent dynamic critical exponent. In the case of a liquid–vapor transition, the quantity analogous to $D_\mathrm{m}$ is the thermal conductivity $D_T$, bearing the same critical exponent as $\tau \to 0$.

Transport mechanisms in near-critical fluids have to respect hydrodynamic conservation laws, specifically for mass, momentum, and internal energy. The dynamics of one-component fluids undergoing a liquid–vapor transition is described by the so-called model $H$ [6, 20], which incorporates the conservation of a scalar order parameter and of the transverse part of the momentum current. The asymptotic behaviors for $\tau \to 0$ of the thermal conductivity and of the shear viscosity in model $H$ have been well studied and the corresponding critical exponents for this universality class are known [6]. A binary liquid mixture, on the other hand, can exhibit two kinds of transitions: liquid–vapor transitions at plait points and demixing transitions at consolute points. Unlike a one-component fluid, for a binary liquid mixture there are two conserved scalar fields, viz., the concentration field and the density field. Critical dynamics in binary liquid mixtures are described by model $H'$ [6]. The transport properties are reported [21] to exhibit different features at the consolute and the plait points. For example, for $\tau \to 0$ the thermal conductivity remains finite at consolute points, but diverges at plait points of a binary liquid mixture [21, 22]. Moreover, also the corresponding behaviors in the non-asymptotic regime are quite different. However, in the asymptotic regimes the leading critical exponents (including the dynamic ones) at the consolute points of a binary mixture are the same as the ones for a one-component fluid [6]. The to date best estimate for $x_\eta \approx 0.068$ in $d = 3$ was obtained within a self-consistent mode-coupling approximation for a one-component fluid [23] and is in agreement with previous theoretical calculations [4, 17, 21, 24–26]; it is also corroborated by experiments on xenon near its liquid–vapor critical point [27]. By virtue of universality and using Eq. (7), this implies for the dynamic critical exponents of model $H'$ in $d = 3$ [6]:

$$x_\eta \approx 0.068\,,\ x_D \approx 1.068\,,\ \text{and}\ z \approx 3.068\,. \tag{8}$$

The presence of the density as a secondary fluctuating field, which is coupled to the order parameter field (i.e., the concentration) through some constraint [cf. Eq. (19)], generally raises the question whether Fisher renormalization [28] has to be accounted for. For the present study of symmetric binary mixtures, we have no indications that this is the case, but this issue deserves further theoretical investigation.

Compared with the large body of research on static critical phenomena, there are relatively few studies on dynamic critical phenomena. Concerning theory, they are performed mainly by using *mode-coupling* theory (MCT) [29, 30] or *dynamic renormalization group* theory(RGT) [31, 32] (see Refs. [6, 18] for recent reviews). In parallel to that, the phenomenological *dynamic scaling* formalism [33] has also been used extensively. There are important experimental observations (see, e.g., Refs. [9, 27, 34, 35]) which have pushed the development of this research area.

On the other hand, there are only few computational studies on dynamic critical phenomena [36–38]. Such kind of computer simulations for fluids started only a decade ago. The first MD simulation [36] aiming at the critical singularities in the fluid transport quantities was performed in 2004. Although this study produced the correct values of the static

critical exponents for the susceptibility and the correlation length, the reported critical exponent for the interdiffusivity was in disagreement with theoretical predictions. There are numerical studies [39, 40] of shear and bulk viscosities close to the liquid–vapor transitions of one-component fluids too, but, without characterizing quantitatively their critical singularities. The first quantitative determinations of critical exponents and amplitudes for transport in fluids—being in accordance with MCT, dynamic RGT, and experiments—were performed by Das *et al.* in 2006 by using MD simulations [41–43]. Applying finite-size scaling theory [44], the critical singularities of the shear viscosity, of the Onsager coefficient, and of the mutual diffusivity were determined. Along these lines, the critical divergence of the bulk viscosity was determined recently [38, 45] for a demixing phase transition. In this context, we are aware of only one simulation study [37] of the dynamic critical exponents associated with liquid–vapor transitions (model $H$). Also, there are no studies of dynamic critical phenomena below $T_c$. The latter ones are complicated by non-standard finite-size effects changing the location of the binodals [45], along which the transport quantities have to be calculated.

Simulations of dynamic critical phenomena face particular challenges such as, inter alia, critical slowing down [17] and finite-size effects. While upon increasing the system size finite-size effects become less pronounced, the critical slowing down ($t_r \sim \xi^z \sim \tau^{-\nu z} \to \infty$) causes simulations of large systems to become expensive due to increasing equilibration times. This leads to noisy simulation data for any transport property near criticality at which large scale fluctuations are unavoidable and thus make the determination of critical singularities very difficult. This problem is even more pronounced for quantities associated with collective dynamics, such as the shear viscosity, which lack the self-averaging of tagged-particle quantities. Critical slowing down also manifests itself in long-time tails of the Green-Kubo correlators of transport quantities. In particular, for the bulk viscosity, this has been demonstrated [38, 39, 45] to make the computation notoriously difficult. Moreover, there are also technical hurdles concerning the temperature control [46, 47] during long MD runs near $T_c$. One way of dealing with these problems is to carry out MD simulations of smaller systems and then to apply a finite-size scaling analysis, as done in Refs. [38, 41, 42, 45]. However, in the present study we deal with huge system sizes such that the use of finite-size scaling is less important for determining the relevant critical singularities.

This study is organized such that in Section II various models considered here and the simulation methodologies are described. Section III contains the results for various static and dynamic quantities. There, we also compare our computational observations with available theoretical and experimental predictions. Finally, in Section V, we provide a summary and perspectives.

## II. MODELS AND METHODS

### A. Models

As model fluids, we have considered binary mixtures of A and B particles, which interact via the Lennard-Jones (LJ) pair potential

$$u^{\mathrm{LJ}}(r;\varepsilon,\sigma) = 4\varepsilon\left[(\sigma/r)^{12} - (\sigma/r)^{6}\right]. \tag{9}$$

Particles of species $\alpha,\beta \in \{\mathrm{A},\mathrm{B}\}$ have different interaction strengths $\varepsilon_{\alpha\beta}$, while for reasons of simplicity all particles share the same diameter $\sigma$ and mass $m$. The actually employed pair potentials are

$$u_{\alpha\beta}(r) = [u^{\mathrm{LJ}}_{\alpha\beta}(r;\varepsilon_{\alpha\beta},\sigma) - u^{\mathrm{LJ}}_{\alpha\beta}(r_c;\varepsilon_{\alpha\beta},\sigma)]f\left(\frac{r-r_c}{h}\right), \tag{10}$$

where the potential is smoothly truncated at a suitable cut-off distance $r_c$ for computational benefits such that the pair force is still continuously differentiable at $r = r_c$. We used the smoothing function $f(x) = x^4\theta(-x)/(1+x^4)$, where $\theta$ is the Heaviside step function [48, 49]. A small value of $h = 0.005\sigma$ is sufficient to ensure very good numerical stability with respect to conservation laws during long MD runs [50], which is indispensable for the study of critical dynamics of molecular fluids.

Throughout, we have used cubic simulation boxes of edge length $L$ and volume $V = L^3$ with periodic boundary conditions applied along all Cartesian directions. The total number density $\varrho = N/V$ is kept constant, where $N = N_{\mathrm{A}} + N_{\mathrm{B}}$ is the total number of particles and $N_\alpha$ is the number of particles of species $\alpha$. With this, the concentration is defined as $x_\alpha = N_\alpha/N$. We adopt $\varepsilon_{\mathrm{AA}} = \varepsilon$ as the unit of energy. In turn this sets the dimensionless temperature $T^* = k_{\mathrm{B}}T/\varepsilon$. For the choice $\varepsilon_{\mathrm{AA}} = \varepsilon_{\mathrm{BB}}$ the binary liquid mixture is symmetric. This symmetry leads to several computational advantages concerning the calculation of the phase diagram [15] and improves the statistics of single-particle averages. The various fluids considered here are specified by their set of parameters ($\varepsilon_{\mathrm{AB}}$, $r_c$, $\varrho$) to be described next.

As to model I, we choose

$$r_{c,\alpha\beta} = 2.5\sigma, \qquad \varepsilon_{\mathrm{AA}} = \varepsilon_{\mathrm{BB}} = \varepsilon, \qquad \varepsilon_{\mathrm{AB}} = \frac{\varepsilon}{2}, \tag{11}$$

and study various number densities $\varrho$. In model II, we set $r_{c,\alpha\alpha} = 2.5\sigma$ for like-particle interactions ($\alpha = \beta$) and $r_c = 2^{1/6}\sigma$ otherwise, such that the unlike particles interact via the purely repulsive Weeks–Chandler–Andersen (WCA) potential [51]. For this model, we fix

$$\varrho\sigma^3 = 0.8, \qquad \varepsilon_{\mathrm{AA}} = \varepsilon_{\mathrm{BB}} = \varepsilon\,, \tag{12}$$

and keep $\varepsilon_{\mathrm{AB}}/\varepsilon$ as a tunable interaction parameter. Model II is inspired by the Widom–Rowlinson mixture [52], the dynamics of which has been the subject of a recent simulation study [36]. The Lennard-Jones potential [Eq. (9)], and certainly its truncated form [Eq. (10)], decay faster than $r^{-(d+2)}$ as $r \to \infty$ for $d = 3$, which justifies that the critical singularities of static bulk properties belong to the universality class of 3D Ising models with short-ranged interactions.

### B. Semi-grand canonical Monte Carlo simulation

The phase diagram and the static susceptibility $\chi$ are calculated using the semi-grand canonical Monte Carlo (SGMC) [15] simulations. Within SGMC, the total particle number $N$ is kept constant, while $x_A$ and $x_B$ fluctuate. The implementation of the simulation consists of two Monte Carlo (MC) moves: particle displacement and an identity switch $A \rightleftharpoons B$. Due to the identity switch also the chemical potential difference $\Delta\mu = \mu_A - \mu_B$ for the two species enters into the Boltzmann factor. However, for symmetric binary liquid mixtures the coexistence curve below $T_c$ is given by $\Delta\mu = 0$. Accordingly, it is natural to collect the simulation data above $T_c$ also for $\Delta\mu = 0$, which implies that the field conjugate to the demixing order parameter is zero. During the SGMC runs, the concentration $x_A$ has been recorded at sufficiently large intervals of $10^4$ MC steps, so that subsequent samples are approximately independent of each other. For $L = 27$ and $\varrho\sigma^3 = 1.0$, the fluid mixture has been equilibrated over $3 \times 10^6$ MC steps. The attempted particle displacements have been chosen uniformly from the cube $[-\sigma/20, \sigma/20] \times [-\sigma/20, \sigma/20] \times [-\sigma/20, \sigma/20]$.

In the SGMC simulation the concentrations $x_A$ and $x_B$ fluctuate. Therefore the order parameter field $\phi := (x_A - x_B)/2$ is not conserved, but the total number density field is conserved. Accordingly, the SGMC dynamics is classified as the so-called model $C$ with a scalar order parameter [6] and is associated with a dynamic exponent $z_{\mathrm{SGMC}} = 2 + \alpha/\nu \approx 2.175$ (see Table 3 in Ref. [6]). On the other hand, if one performs MC simulations in the canonical ensemble ($N_A$, $N_B$, $V$, and $T$ fixed) with rules such that the order parameter is conserved *locally*- in addition to a conserved density- it corresponds to model $D$. Note that both model D and B correspond to a *locally* conserved order parameter field, with an additional non-critical conserved density field present in model D. It has been shown that the dynamic exponent $z$ for both model B and D as defined above is the same ($z = 4 - \eta \approx 3.964$) [6, 53]. Due to a much smaller value of $z$, MC simulations for model C are computationally faster and more advantageous than for model D. However, the issue of MC simulations in the canonical ensemble with an only globally (not locally) conserved order parameter field, in the presence of a conserved density field, requires further investigations.

### C. Molecular dynamics simulation

Transport quantities have been calculated by using MD simulations [46, 54], which solve Newton's equations of motion for the fluid particles within the microcanonical ensemble ($N_A$, $N_B$, $V$, total momentum, and total energy $E$ fixed). Generically, simulations of critical dynamics are challenged both by critical slowing down and by finite-size effects [15, 17]. Even more so, the study of collective transport requires a sufficient separation of length scales ($\sigma \ll \xi \ll L$). Therefore, we have performed simulations of very large system sizes ($L \leqslant 50\sigma$) containing up to $N = 87{,}500$ particles with the trajectories spanning more than $10^4 t_0$ in time, with $t_0 = \sqrt{m\sigma^2/\varepsilon}$, which is at the high end of the present state of the art.

Such demanding computations have become feasible only recently based on the highly parallel architecture of so-called GPU (graphic processing units) accelerators, which are specialized on streaming numerical computations of large data sets in parallel. The success of GPU computing in the realm of MD simulations [55] has stimulated the development of GPU implementations for more advanced algorithms [56], and today such accelerator hardware is often part of new installations in high-performance computing centers. Specifically, we have used the software *HAL's MD package* (version 1.0) [50, 57], which is a high-precision molecular dynamics package for large-scale simulations of complex dynamics in inhomogeneous liquids. The implementation achieves excellent conservation of energy and momentum at high performance by using an increased floating-point precision where necessary [50, 58]. The software minimizes disk usage by the *in situ* evaluation of thermodynamic observables and dynamic correlation functions and by writing structured, compressed, and portable H5MD output files [59]. Concerning the performance of the package, it has been shown to reliably reproduce the slow glassy dynamics of the Kob–Andersen mixture [50], and it was used recently to shed new light on the structure of liquid–vapor interfaces [60].

For the thermalization of the initial state, we have used a Nosé–Hoover thermostat (NHT) chain [46, 61] with an integration time step of $\delta t = 0.002 t_0$. We note that NHT dynamics has recently been demonstrated [47] to generate critical transport in binary liquid mixtures within the universality class of model $H'$. We have applied the following equilibration procedure: *(i)* Generate an initial lattice configuration with the desired particle numbers $N_A$, $N_B$, and the volume $V$ such that the two species of the particles are randomly assigned and that the total momentum is zero. *(ii)* Melt this lattice at the temperature $2T$ for $100 t_0$ using the NHT and further equilibrate it at $T$; typical run lengths are $t = 10^4 t_0$ for $L = 42\sigma$ and $\varrho\sigma^3 = 1.0$. *(iii)* Determine the average internal energy $U$ at $T$ from the previous NHT run and rescale the particle velocities such that the instantaneous total energy matches $U$. The resulting system state is used to compute transport quantities in a production run at fixed total energy, employing the velocity Verlet algorithm with an integration time step of $\delta t = 0.001 t_0$. For model II with $\varepsilon_{AB}/\varepsilon = 1$ we have used $\delta t = 0.0005 t_0$. These choices for $\delta t$ result in a relative energy drift of less than $2 \times 10^{-5}$ in $1.5 \times 10^7$ steps.

### D. Data acquisition and statistics

All results presented in the following correspond to the critical composition $x_c = 1/2$ and $T^* \geq T_c^*$. Unless stated otherwise, static quantities are all averaged over 20 independent initial configurations and for dynamic quantities this number is 30. During the production runs in the NVE ensemble (i.e., $N_A$, $N_B$, $V$, and $E$ constant), data are recorded over a time span of $t = 15{,}000\, t_0$. For example, the computing time for a system trajectory of 74,088 particles over $1.5 \times 10^7$ steps, using a single Tesla K20Xm GPU (NVIDIA Corp.), was 7.1 h at the wall clock, including the evaluation of static and dynamic

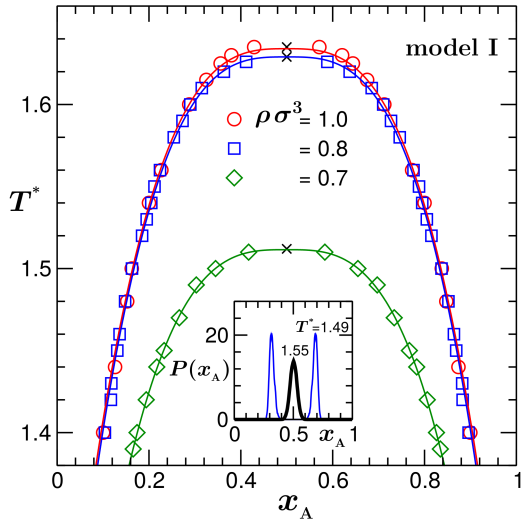


FIG. 1. Demixing phase diagrams in the $x_A$–$T^*$ plane for binary liquid mixtures within model I for 3 number densities $\varrho$ [$x_A = N_A/(N_A + N_B)$ and $T^* = k_B T/\varepsilon$ with $\varepsilon = \varepsilon_{AA}$]. Open symbols indicate co-existing equilibrium states obtained from SGMC simulations. Solid lines are fits to these data yielding estimates for $T_c(\varrho)$ (see the main text), and crosses mark the critical points $(x_c = 1/2, T_c)$. The chosen system sizes are $L = 27\sigma$, $29\sigma$, and $30\sigma$ for $\varrho\sigma^3 = 1.0$, 0.8, and 0.7, respectively. In all cases, the statistical errors do not exceed the symbol sizes. The inset shows the probability density $P(x_A)$ for model I at $\varrho\sigma^3 = 0.7$, $L = 30\sigma$, and two values of $T^*$.

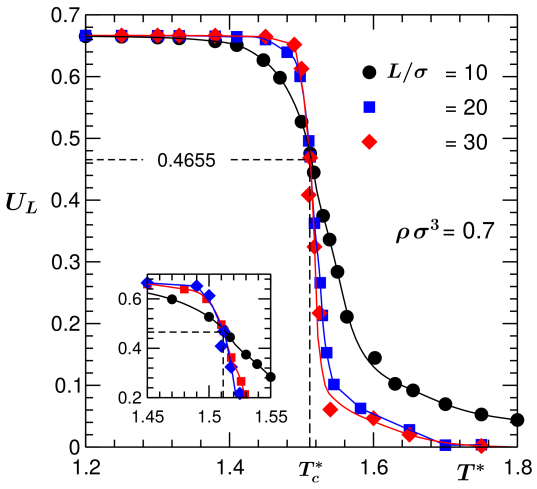


FIG. 2. Binder cumulant $U_L(T)$ [Eq. (15)] for model I with $\varrho\sigma^3 = 0.7$ and for 3 values of $L$. The solid lines are interpolating weighted splines and the dashed lines mark the common intersection point. The inset provides an enlarged view of the neighbourhood of the intersection point at $T_c^*$.

correlations.

## III. RESULTS

### A. Phase diagrams

From the SGMC simulations we have obtained the demixing phase diagrams for the 5 fluids studied. For each fluid, the probability density $P(x_A)$ of the fluctuating concentration $x_A$ of A particles has been determined at various dimensionless temperatures $T^*$ above and below the anticipated demixing point; $P(x_A)$ is normalized: $\int_0^1 P(x_A)\,\mathrm{d}x_A = 1$. In a finite system of linear size $L$ with periodic boundary conditions along all directions the critical transition is shifted and rounded, following the finite-size scaling relation $T_c(L \to \infty) - T_c \sim L^{-1/\nu}$ [44]. In our simulations, we have used large values for $L$ so that the finite-size effects are sufficiently small. The inset of Fig. 1 shows results for $P(x_A)$ for model I with $\varrho\sigma^3 = 0.7$ and for two exemplary temperatures: $P(x_A)$ shows a single peak above $T_c^L$ and assumes a double-peak structure below $T_c^L$. These peaks of $P(x_A)$ correspond to equilibrium states because, up to an $x_A$-independent constant, the free energy is given by $-k_B T \log(P(x_A))$. Accordingly, the two peaks of equal height indicate the coexistence of an A- and a B-rich phase below $T_c^L$. Due to the symmetry of the binary liquid mixtures, one has $P(x_A) = P(1 - x_A)$, which we have imposed on the data for $P(x_A)$. Therefore, the critical composition is $x_{A,c} = x_{B,c} = x_c = 1/2$ which holds exactly for all the models considered by us here.

Accordingly, the fluctuating order parameter is given by $\phi = x_A - 1/2$, from which we have calculated the mean order parameter $\varphi$ as

$$\varphi = \langle|\phi|\rangle = \int_0^1 \left|x_A - 1/2\right| P(x_A)\,\mathrm{d}x_A\,. \tag{13}$$

Below $T_c$, where $\varphi > 0$, the binodal is given by the coexisting concentrations $x_A^{(1,2)}(T) = 1/2 \pm \varphi(T)$. The results are shown in Fig. 1, and one expects that they follow the asymptotic power law

$$\varphi(T \nearrow T_c) \simeq \varphi_0\,|T/T_c - 1|^{\beta}\,, \tag{14}$$

which defines also the amplitude $\varphi_0$. However, deviations are expected to occur for $T$ very close to $T_c$ due to the finite-size effects mentioned before [38, 62]. For each of the 5 fluids studied, $T_c$ and $\varphi_0$ have been estimated via fits of Eq. (14) to the data, with $\beta = 0.325$ fixed [Eq. (3)]. Ideally, all three parameters $(\varphi_0, \beta, T_c)$ can be obtained from a single fit procedure as described above. However, trying to extract an unknown exponent close to $T_c$ from data for finite-sized systems is a delicate task which usually leads to large uncertainties. Already for the extraction of $\varphi_0$ and $T_c$ alone one has to choose the fit range judicially: data points very close to $T_c$ suffer from finite-size effects, while the asymptotic law is not expected to hold at temperatures far away from $T_c$. Exemplarily for $\varrho\sigma^3 = 0.7$, we have chosen $x_A \in (0.2, 0.4)$. Surprisingly, the power law in Eq. (14) provides a good description of the binodal even at temperatures well below $T_c$.

We have refined the estimates for $T_c$ with Binder's intersection method [13, 14]. It is based on the dimensionless

cumulant

$$U_L(T) = 1 - \frac{\langle \phi^4 \rangle}{3 \langle \phi^2 \rangle^2}, \tag{15}$$

which interpolates between the limiting values $U_L(T \to 0) = 2/3$ and $U_L(T \to \infty) = 0$ and, at $T_c$, it attains a universal value $U_L(T_c)$ for sufficiently large $L$. Plotting $U_L(T)$ vs. $T$ for various system sizes $L$, the set of curves exhibits a common point of intersection, from which one infers an accurate estimate for $T_c$. This is demonstrated in Fig. 2, showing a family of intersecting curves $U_L(T)$ for model I with $\varrho\sigma^3 = 0.7$ and for three values of $L$. The figure corroborates the critical value $U_L(T_c) \approx 0.4655$ [14] for the Ising universality class, from which we read off $T_c^* = 1.5115 \pm 0.0008$.

The main results for all 5 fluids studied here have been compiled in Table I. For model II, we have found much higher values for $T_c$ than for model I. This can be understood as follows. The AA and BB interaction potentials are identical both within and between the two models, which differ only with respect to the AB interaction potential. Upon construction [see Eq. (10)], the AB interaction is more repulsive in model II than in model I ($u_{\mathrm{AB}}^{\mathrm{II}}$ is purely repulsive whereas $u_{\mathrm{AB}}^{\mathrm{I}}$ exhibits also an attractive part). A repulsive AB interaction favors the formation of domains rich in A and of domains rich in B and thus promotes demixing, which leads to a higher value of $T_c$. Within model II, increasing $\varepsilon_{\mathrm{AB}}$ makes $u_{\mathrm{AB}}^{\mathrm{II}}$ more repulsive and thus renders the same trend. In particular, increasing within model II the attraction strength $\varepsilon_{\mathrm{AB}}$ by a factor of 4 yields an 1.7-fold increase of $T_c$. The binodal for model II with $\varepsilon_{\mathrm{AB}}/\varepsilon = 1$ (but $u_{\alpha\alpha}$ truncated at $r_c/\sigma = 4.2$) was determined in Ref. [63], and the rough estimate of $T_c$ there agrees with our result. Model I was studied by Das *et al.* [62] for $\varrho\sigma^3 = 1.0$, but using sharply truncated interaction potentials [$f(x) \equiv \theta(-x)$ in Eq. (10)]. They found $T_c^* = 1.638 \pm 0.005$, which is very close to our result $T_c^* = 1.635 \pm 0.003$, however different from $T_c^* \approx 1.423$ as obtained for the force-shifted potentials used in Ref. [42]. We propose that this difference appears because the smoothing function $f(x)$ alters $u_{\alpha\beta}(r)$ only locally near $r_c$, unlike the force shift which amounts to modify the interaction potentials globally. Within model I, the amplitude $\varphi_0$ of the order parameter is, within the accuracy of our data, insensitive to the density $\varrho$ (see Table I). Within model II, $\varphi_0$ changes only slightly upon increasing the strength $\varepsilon_{\mathrm{AB}}$ of the repulsion.

The dependence of the demixing transition on the total number density $\varrho$ gives rise to a line $T_c(\varrho)$ of critical points, known as the *λ-line* (Fig. 3). For model I, we have found that $T_c(\varrho)$ is an increasing function for $\varrho\sigma^3 \lesssim 0.9$; for higher densities, it decreases. Such a non-monotonic dependence implies a re-entrance phenomenon: increasing the density isothermally, the binary liquid mixture undergoes a phase transition from a mixed state at low density to a phase-separated one and mixes again at high densities.

The initial increase of $T_c(\varrho)$ is in qualitative agreement with a previous grand-canonical MC study [64] using a variant of our model I ($\varepsilon_{\mathrm{AB}} = 0.7\varepsilon_{\mathrm{AA}}$). For this choice of the interaction potentials, it was found that the $\lambda$-line ends at a critical end point near $\varrho\sigma^3 \approx 0.59$, where the $\lambda$-line hits the first-order liquid–vapor transition of the fluid. It was suggested [64] that upon decreasing $\varepsilon_{\mathrm{AB}}$ further the critical end point moves towards the line of liquid–vapor critical points until both lines of critical points meet for $\varepsilon_{\mathrm{AB}} \approx 0.6\varepsilon_{\mathrm{AA}}$ and form a tri-critical point, as observed in a two-dimensional spin model [16]. The determination of the full phase diagrams of binary liquid mixtures, encompassing the complete $\lambda$-line, the line of liquid–vapor critical points, and the solid phases, is a non-trivial and computationally demanding task (for density functional approaches in this direction see Refs. [65–67]). It remains as an open question whether there is a tri-critical point in model I ($\varepsilon_{\mathrm{AB}} = 0.5\varepsilon_{\mathrm{AA}}$) or not (see below for further discussions).

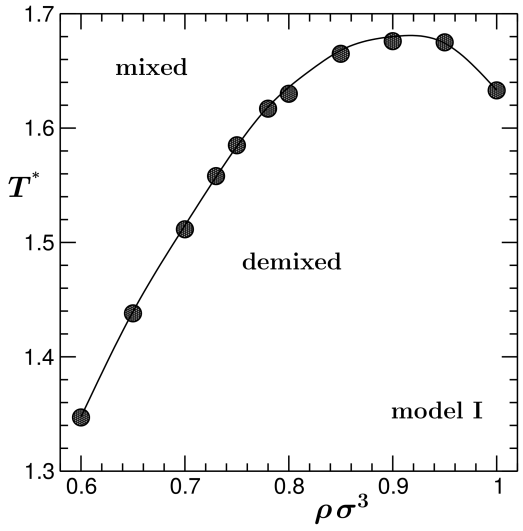


FIG. 3. Loci of the critical points $T_c(\varrho)$ for the demixing transition in the $\varrho$–$T^*$ plane with $T^* = k_{\mathrm{B}}T/\varepsilon$, obtained from SGMC simulations for model I. The solid line is an interpolating weighted spline. For details of the interaction potentials, see the main text and Table I. Error bars are smaller than the symbol sizes.

For completeness, Table I also lists the critical values for the dimensionless pressure $P_c^* = P_c\sigma^3/\varepsilon$ at the respective demixing points, which have been obtained, following the standard procedures for a homogeneous and isotropic fluid, from the trace of the time-averaged stress tensor, $P = \mathrm{tr}\,\langle \Pi(t) \rangle /3V$, with the instantaneous stress tensor given by [68]

$$\Pi(t) = \sum_{i=1}^{N} \left\{ m\mathbf{v}_i(t) \otimes \mathbf{v}_i(t) + \sum_{j>i}^{N} \mathbf{r}_{ij}(t) \otimes \mathbf{F}_{ij}(t) \right\}, \tag{16}$$

where $\mathbf{v}_i(t)$ is the velocity of particle $i$, $\mathbf{r}_{ij}(t) = \mathbf{r}_i(t) - \mathbf{r}_j(t)$, $\mathbf{F}_{ij}(t)$ is the force acting on particle $j$ due to particle $i$, and $\otimes$ denotes a tensor product. We also specify the internal energy per particle,

$$U = \frac{1}{N} \sum_{i=1}^{N} \left\langle \frac{m}{2} \mathbf{v}_i(t)^2 + \sum_{j>i}^{N} u_{\alpha_i\alpha_j}(|\mathbf{r}_{ij}(t)|) \right\rangle, \tag{17}$$

at the critical points, which characterizes the microcanonical ensemble probed by MD simulations; $\alpha_i \in \{A, B\}$ denotes the species of particle $i$.

| | model I | | | model II | | Ref. [42] |
|---|---|---|---|---|---|---|
| $\varrho\sigma^3$ | 0.7 | 0.8 | 1.0 | 0.8 | 0.8 | 1.0 |
| $\varepsilon_{AB}/\varepsilon$ | 1/2 | 1/2 | 1/2 | 1/4 | 1 | 1/2 |
| $r_{c,AB}/\sigma$ | 2.5 | 2.5 | 2.5 | $2^{1/6}$ | $2^{1/6}$ | 2.5 + force shift |
| $T_c^*$ | 1.5115(8) | 1.629(1) | 1.635(3) | 2.608(2) | 4.476(2) | 1.4230(5) |
| $P_c^*$ | 2.58(5) | 4.81(3) | 12.70(4) | 8.29(5) | 16.31(6) | |
| $U_c/\varepsilon$ | −0.617(3) | −0.584(3) | −0.572(4) | 2.643(4) | 6.557(6) | |
| $\kappa_c^*$ | 0.11(4) | 0.05(3) | 0.02(3) | 0.04(4) | 0.02(4) | |
| $\varphi_0$ | 0.76(2) | 0.77(2) | 0.745(16) | 0.77(3) | 0.70(2) | 0.765(25) |
| $\chi_0^*$ | 0.157(9) | 0.112(7) | 0.068(4) | 0.056(4) | 0.06(2) | 0.076(6) |
| $\xi_0/\sigma$ | 0.53(3) | 0.47(2) | 0.42(2) | 0.45(3) | 0.53(2) | 0.395(25) |
| $R_\xi^+ R_c^{-1/d}$ | 0.71(7) | 0.70(6) | 0.72(6) | 0.72(8) | 0.65(9) | 0.69(8) |
| $\eta_0^*$ | | 1.46(10) | 3.63(10) | 1.35(5) | 1.80(7) | 3.87(30) |
| $\mathscr{L}_0^*$ | 0.0143(5) | 0.0082(4) | 0.0024(3) | 0.0049(4) | 0.0032(4) | 0.0028(4) |
| $\mathscr{L}_{\mathrm{b},0}^*$ | 0.0082(7) | 0.0040(6) | 0.0028(4) | 0.0025(5) | 0.0013(7) | 0.0033(8) |
| $D_{m,0}^*$ | 0.091(8) | 0.073(6) | 0.035(5) | 0.088(7) | 0.053(6) | 0.037(8) |
| $R_D$ | | 0.95(17) | 0.993(21) | 1.00(21) | 0.96(25) | 1.06(40) |

TABLE I. Simulation results for the five binary fluids investigated here along with results from Ref. [42]: values of the critical temperature $T_c$ and of the pressure $P_c$, the internal energy $U_c$ [Eq. (17)], and the isothermal compressibility $\kappa_c$ at the critical point; further, the critical amplitudes of the correlation length $\xi_0$ [Eq. (22)], of the order parameter $\varphi_0$, and of the static susceptibility $\chi_0$ [Eq. (22)], as well as of the shear viscosity $\eta_0$ [Eqs. (34) and (35)] and the Onsager coefficient $\mathscr{L}_0$ [Eqs. (27)–(29)]. The amplitudes $D_{m,0}$ of the interdiffusion constant have been computed from Eq. (33). Finally, the values of two universal ratios of static and dynamic amplitudes, $R_\xi^+ R_c^{-1/d}$ and $R_D$ [see Eqs. (39) and (40), respectively], are reported. Numbers in parentheses indicate the uncertainty in the last digit(s).

### B. Spatial correlations

#### 1. *Static structure factors*

The structural properties of binary liquid mixtures arise from the two fluctuating fields, given by the microscopic partial number densities $\varrho_\alpha(\mathbf{r})$ of each species $\alpha$. Their fluctuating parts are [68]

$$\delta\varrho_\alpha(\mathbf{r}) = -\frac{N_\alpha}{V} + \sum_{j=1}^{N_\alpha} \delta\big(\mathbf{r} - \mathbf{r}_j^{(\alpha)}\big)\,, \tag{18}$$

where the set $\{\mathbf{r}_j^{(\alpha)}\}$ denotes the positions of the $N_\alpha$ particles of species $\alpha$. It is favorable to (approximately [62]) decouple the spatial fluctuations into the overall density contribution $\delta\varrho(\mathbf{r})$ and into the composition contribution $\delta c(\mathbf{r})$ and, accordingly, to consider the linear combinations [69]

$$\delta\varrho(\mathbf{r}) = \delta\varrho_\mathrm{A}(\mathbf{r}) + \delta\varrho_\mathrm{B}(\mathbf{r}) \tag{19a}$$

and

$$\delta c(\mathbf{r}) = x_\mathrm{B}\delta\varrho_\mathrm{A}(\mathbf{r}) - x_\mathrm{A}\delta\varrho_\mathrm{B}(\mathbf{r})\,; \tag{19b}$$

$\delta\varrho(\mathbf{r})$ fluctuates around the total density $\varrho = (N_\mathrm{A} + N_\mathrm{B})/V$. In Fourier space, the corresponding spatial correlation functions are defined as

$$S_{\varrho\varrho}(|\mathbf{k}|) = \frac{1}{N}\left\langle \delta\varrho_\mathbf{k}^* \, \delta\varrho_\mathbf{k} \right\rangle, \tag{20a}$$

$$S_{cc}(|\mathbf{k}|) = N\left\langle \delta c_\mathbf{k}^* \, \delta c_\mathbf{k} \right\rangle, \tag{20b}$$

and

$$S_{\varrho c}(|\mathbf{k}|) = \mathrm{Re}\left\langle \delta\varrho_\mathbf{k}^* \, \delta c_\mathbf{k} \right\rangle, \tag{20c}$$

where, e.g., $\delta\varrho_\mathbf{k} = \int_V \mathrm{e}^{\mathrm{i}\mathbf{k}\cdot\mathbf{r}}\delta\varrho(\mathbf{r})\,\mathrm{d}^3r$ and, see below, $\delta\varrho_\mathbf{k}^{(\alpha)} = \int_V \mathrm{e}^{\mathrm{i}\mathbf{k}\cdot\mathbf{r}}\delta\varrho_\alpha(\mathbf{r})\,\mathrm{d}^3r$.

On the fly of the MD simulations, we have determined the partial structure factors $S_{\alpha\beta}(|\mathbf{k}|) = (f_{\alpha\beta}/N)\left\langle \delta\varrho_{-\mathbf{k}}^{(\alpha)} \, \delta\varrho_\mathbf{k}^{(\beta)} \right\rangle$, where $f_{\alpha\beta} = 1$ for $\alpha = \beta$ and $f_{\alpha\beta} = 1/2$ for $\alpha \neq \beta$ [68], which allow one to determine

$$S_{\varrho\varrho}(k) = S_\mathrm{AA}(k) + S_\mathrm{BB}(k) + 2S_\mathrm{AB}(k)\,, \tag{21a}$$

$$S_{cc}(k) = x_\mathrm{B}^2 S_\mathrm{AA}(k) + x_\mathrm{A}^2 S_\mathrm{BB}(k) - 2x_\mathrm{A}x_\mathrm{B}S_\mathrm{AB}(k)\,, \tag{21b}$$

and

$$S_{\varrho c}(k) = x_\mathrm{B}S_\mathrm{AA}(k) - x_\mathrm{A}S_\mathrm{BB}(k) + (x_\mathrm{B} - x_\mathrm{A})\,S_\mathrm{AB}(k)\,. \tag{21c}$$

Here, we are primarily interested in the critical fluctuations of the composition, which are borne out by $S_{cc}(k)$ for small $k$. The latter is of the (extended) Ornstein–Zernike form [2, 68]

$$S_{cc}(k) \simeq \frac{\varrho k_\mathrm{B}T\chi}{[1 + k^2\xi^2]^{1-\eta/2}}\,, \quad k\sigma \ll 1\,, \tag{22}$$

which defines both the static order parameter susceptibility $\chi \sim \tau^{-\gamma}$ and the correlation length $\xi \sim \tau^{-\nu}$ which in real space governs the exponential decay of the correlation functions. The anomalous dimension $\eta \approx 0.036$ follows from the exponent relation $\gamma = \nu(2-\eta)$ [5] and the values in Eq. (3). Exemplary results for $S_{cc}(k)$ and $S_{\varrho\varrho}(k)$ are shown in Fig. 4, for model I with $\varrho\sigma^3 = 0.7$, on double-logarithmic scales. For the studied range

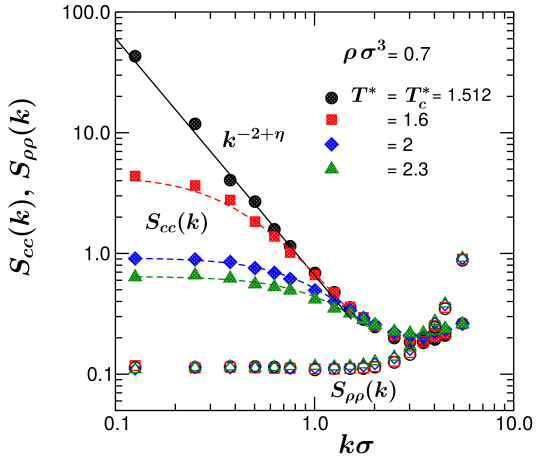


FIG. 4. Static structure factors $S_{cc}(k)$ (filled upper symbols) and $S_{\varrho\varrho}(k)$ (open lower symbols) for model I ($\varrho\sigma^3 = 0.7$, $L = 50\sigma$) at four dimensionless temperatures $T^* \geqslant T_c^* = 1.512$ [see Eq. (20)]. The dashed lines show fits to the extended Ornstein–Zernike form [Eq. (22)] for $T > T_c$. The solid line indicates the critical law $S_{cc}(k, T = T_c) \sim k^{-2+\eta}$, $\eta = 0.036$, which appears as a straight line on the double-logarithmic scales. Error bars are of the size of the symbols.

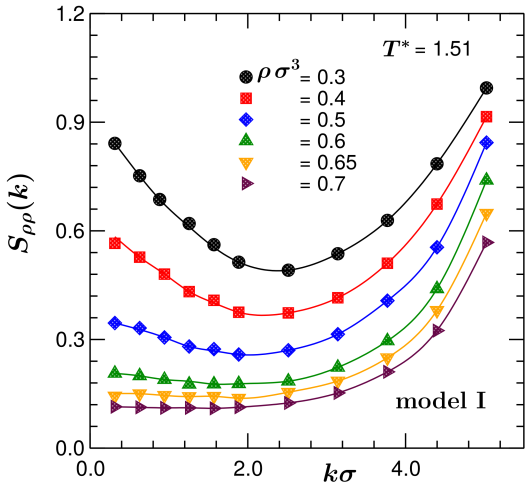


FIG. 5. Static structure factor $S_{\varrho\varrho}(k)$ for model I ($L = 20\sigma$) for six number densities $\varrho$ and fixed dimensionless temperature $T^* = 1.51$. Lines are drawn by using suitable splines.

of temperatures, $T_c^* \leqslant T^* \leqslant 2.3$, all curves for $S_{cc}(k)$ display a minimum near $k\sigma \approx 3$ and are not sensitive to temperature for $k$ larger than this. $S_{cc}(k)$ increases as $k \to 0$, which, due to the divergence of $\chi \sim \tau^{-\gamma}$ at $T_c$, becomes stronger as $T \to T_c$. This reflects the enhancement of the critical composition fluctuations with a concomitant increase of the correlation length $\xi$. The data for $S_{cc}(k)$ for $T > T_c$ exhibit a nice consistency with the theoretical extended Ornstein–Zernike form, depicted by the dashed lines in Fig. 4, over approximately one decade in wavenumber $k$. Right at $T_c$, the data for $S_{cc}(k)$ follow for one decade in $k$ the expected critical power law [2]

$$S_{cc}(k \to 0, T = T_c) \sim k^{-2+\eta}, \tag{23}$$

emerging from Eq. (22) for $k\xi \gg 1$.

To the contrary, the density fluctuations, described by $S_{\varrho\varrho}(k)$, do not change appreciably within the temperature range considered (Fig. 4). There is no critical enhancement for small wave numbers and the spatial range of the density–density correlations is short near the demixing transition with $\varrho\sigma^3 = 0.7$. The value of $S_{\varrho\varrho}(k \to 0) = \varrho k_B T \kappa_T$ yields the isothermal compressibility $\kappa_T = \kappa_T^* \sigma^3/\varepsilon$ of the fluid, which diverges at a liquid–vapor critical point. Along the $\lambda$-line $T_c(\varrho)$, it increases from $\kappa_c^* := \kappa_T^*(T = T_c) \approx 0.02$ for the highly incompressible fluid at $\varrho\sigma^3 = 1$ to $\kappa_c^* \approx 0.11$ at $\varrho\sigma^3 = 0.7$ (Table I). In all cases one has $S_{\varrho\varrho}(k \to 0) \ll S_{cc}(k \to 0)$. From this we conclude that, for the densities considered here, the liquid–vapor and the demixing critical points are sufficiently well separated.

In order to probe the location of the line of the liquid–vapor critical points, we have lowered the density along the isotherm $T^* = 1.51 \approx T_c^*(\varrho\sigma^3 = 0.7)$. Indeed, for $\varrho\sigma^3 \lesssim 0.6$ the corresponding structure factors $S_{\varrho\varrho}(k)$, shown in Fig. 5, display the emergence of critical density fluctuations via a monotonic

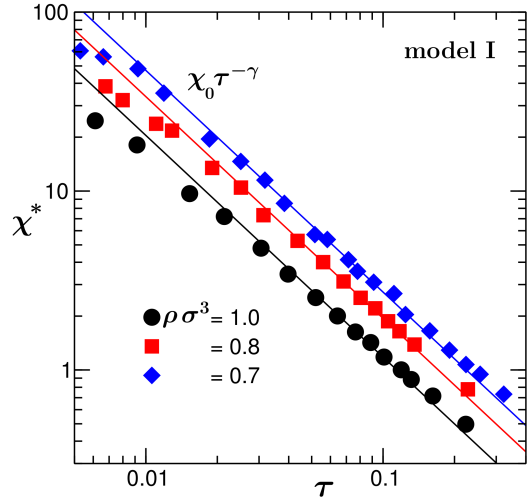


FIG. 6. Reduced static order parameter susceptibility $\chi^* = \chi\varepsilon\sigma^{-3}$ [Eqs. (22) and (24)] as function of $\tau = (T - T_c)/T_c$ within model I for three number densities. The system sizes are $L/\sigma = 42, 47$, and 50 for $\varrho\sigma^3 = 1.0, 0.8$, and 0.7, respectively. Straight lines indicate the asymptotic power law $\chi(T \to T_c) \simeq \chi_0\tau^{-\gamma}$ with $\gamma = 1.239$. Error bars are smaller than the symbol sizes.

increase of the compressibility by a factor of 19. Further, the value of $\kappa_T^*(\varrho\sigma^3 = 0.3, T^* = 1.51)$ is ca. 7.4 times larger than $\kappa_c^* \simeq 0.25$ at $T_c(\varrho\sigma^3 = 0.6)$, following the $\lambda$-line (Fig. 3). This suggests that $\kappa_T^*$ does not diverge along the $\lambda$-line, which implies that the $\lambda$- line and the line of liquid–vapor critical points do not meet, thus rendering the occurrence of a tricritical point in model I as to be unlikely.

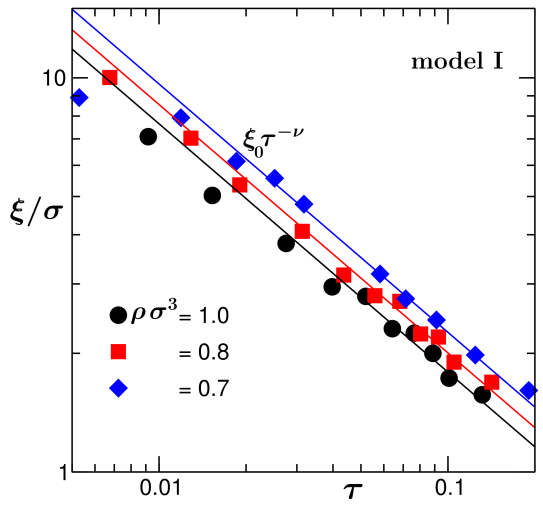


FIG. 7. Correlation length $\xi$ of the concentration fluctuations [Eqs. (22) and (24)] as function of $\tau$ on double-logarithmic scales. Straight lines refer to the asymptotic power law $\xi(T \to T_c) \simeq \xi_0\tau^{-\nu}$ with $\nu = 0.630$. All simulation parameters are the same as in Fig. 6. Relative error bars are within 1 – 9%.

#### 2. *Correlation length and static order parameter susceptibility*

For a broad range of temperatures $T_c \leqslant T \lesssim 2T_c$, we have run extensive MD simulations for three binary liquid mixtures in model I and two binary liquid mixtures in model II. The use of large system sizes has enabled us to reach the critical point as close as $\tau = (T - T_c)/T_c \simeq 0.01$. Fitting Eq. (22) to the data for $S_{cc}(k)$ we have obtained the static order parameter susceptibilities $\chi(T)$ and the correlation lengths $\xi(T)$. The data nicely follow the asymptotic power laws

$$\chi(T \to T_c) \simeq \chi_0\tau^{-\gamma}\,, \qquad \xi(T \to T_c) \simeq \xi_0\tau^{-\nu} \tag{24}$$

near the respective critical temperatures $T_c$ with the Ising critical exponents $\gamma$ and $\nu$ in $d = 3$ (see Figs. 6 and 7 for the binary liquid mixtures in model I). Finite-size effects become apparent for $\tau \lesssim 0.02$, for which the data for both quantities fall short of the asymptotic law. Interestingly, this occurs already for correlation lengths $\xi \approx 4\sigma \approx L/10$. The fit has also identified a temperature range, where corrections to the asymptotic power laws are not yet important. In Fig. 6, the upward trend in $\chi(\tau)$ for $\varrho\sigma^3 = 0.7$ and $\tau > 0.2$ reflects the necessity for such corrections. The amplitudes $\chi_0$ and $\xi_0$ are non-universal quantities and are listed in Table I for each fluid. The trend of a decreasing $\chi_0$ upon increasing $\varrho$ (model I) may be explained by the fact that the re-arrangement of particle positions becomes more costly (in terms of potential energy at denser packing, reducing the response of the system. Even smaller values of $\chi_0$ have been found for model II, with no pronounced dependence on the strength $\varepsilon_{AB}$ of the repulsion. Across all five binary mixtures the amplitude $\xi_0$ of the correlation length varies only mildly between $0.42\sigma$ and $0.53\sigma$.

For comparison, we have also determined the order parameter susceptibility $\chi$ via the SGMC simulations above $T_c$ from the variance of the fluctuating composition [2, 68]. For the symmetric binary liquid mixtures as considered here, one has $\varrho k_B T\chi = N(\langle x_A^2\rangle - \langle x_A\rangle^2)$ with $\langle x_A\rangle = 1/2$ at $T = T_c$ due to the model symmetry and above $T_c$ for the mixed phase. We have found that the results obtained from these two approaches agree.

### C. Transport coefficients

#### 1. *Interdiffusion constant*

A critical point leaves its marks both in space and time: upon approaching criticality the correlation length diverges and the relaxation of a fluctuation or of a perturbation slows down. The latter manifests itself in terms of universal power-law behaviors of transport coefficients upon approaching $T_c$. For example, a gradient in the composition field $\delta c(\mathbf{r}, t)$ [Eq. (19b)] generates a collective current [42, 70, 71]

$$\mathbf{J}_{AB}(t) = x_B \sum_{i=1}^{N_A} \mathbf{v}_i^{(A)}(t) - x_A \sum_{i=1}^{N_B} \mathbf{v}_i^{(B)}(t)\,, \tag{25}$$

the magnitude of which is captured by the interdiffusion constant $D_m$. This coefficient controls the collective diffusion of the composition field and obeys a Green–Kubo relation [42, 70, 71]:

$$D_m = \frac{1}{dNS_{cc}(k=0)} \int_0^\infty \langle \mathbf{J}_{AB}(t) \cdot \mathbf{J}_{AB}(0)\rangle \,\mathrm{d}t\,, \tag{26}$$

where $d$ is the spatial dimension and $S_{cc}(k = 0) = \varrho k_B T\chi$. The interdiffusion constant is a combination of a static property, i.e., the concentration susceptibility $\chi$, and a pure dynamic quantity, the concentration conductivity or Onsager coefficient [42, 70, 71]

$$\mathscr{L} = \chi D_m\,. \tag{27}$$

$\mathscr{L}$ connects gradients in the chemical potentials with the current $\mathbf{J}_{AB}$; as its dimensionless form we use $\mathscr{L}^* := \mathscr{L}\varepsilon t_0\sigma^{-5}$.

The numerical evaluation of the time integral in Eq. (26) is challenged by statistical noise and by hydrodynamic long-time tails of the current correlators [68]. An alternative route to compute $\mathscr{L}$ is based on the generalized Einstein relation [45, 71, 72]

$$\mathscr{L} = \lim_{t\to\infty} \frac{N_\alpha^2}{2\varrho N k_B T} \frac{\mathrm{d}}{\mathrm{d}t}\, \delta\mathscr{R}_\alpha^2(t) \tag{28}$$

for $\alpha \in \{A, B\}$ with the collective mean-square displacement

$$\delta\mathscr{R}_\alpha^2(t) = \left\langle \left| \int_0^t \mathbf{V}_\alpha(t)\,\mathrm{d}t \right|^2 \right\rangle\,, \quad \mathbf{V}_\alpha(t) = \frac{1}{N_\alpha} \sum_{i=1}^{N_\alpha} \mathbf{v}_i^{(\alpha)}(t)\,, \tag{29}$$

defined in terms of the centre-of-mass velocity $\mathbf{V}_\alpha(t)$ by considering particles of species $\alpha$ only. Note that $\mathbf{V}_A(t) = -\mathbf{V}_B(t)$ for a symmetric mixture ($m_A = m_B$, $N_A = N_B$) due to conservation of the total momentum, $\sum_\alpha m_\alpha N_\alpha \mathbf{V}_\alpha = 0$. Our simulation

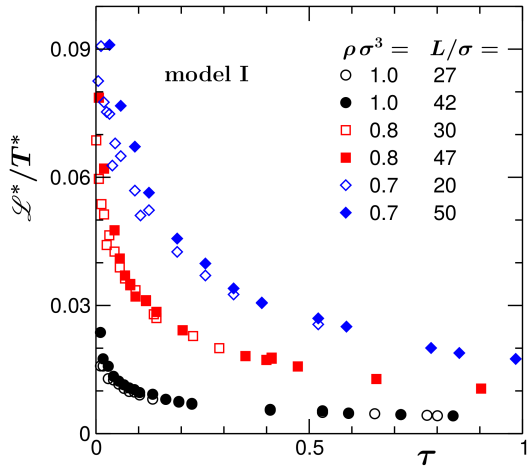


FIG. 8. Plot of $\mathscr{L}^*/T^*$ with $\mathscr{L}^* = \mathscr{L}\varepsilon t_0\sigma^{-5}$ [Eqs. (26)–(29)] for model I as function of the reduced temperature $\tau$, for three number densities $\varrho$. For each $\varrho$, data for two different system sizes $L$ are presented. Relative error bars are within 3–9%.

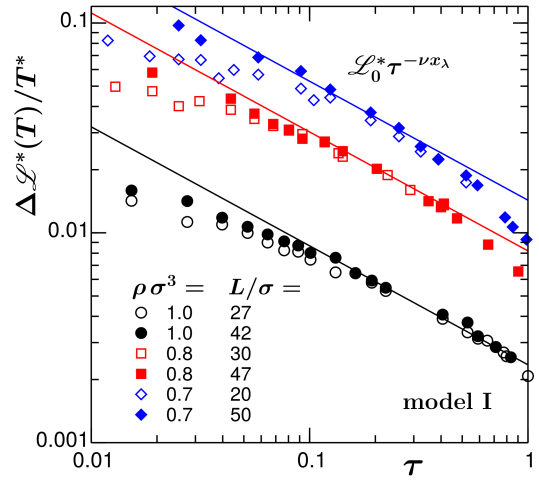


FIG. 9. The same data as in Fig. 8 in terms of $\Delta\mathscr{L}^*/T^* = \mathscr{L}^*/T^* - \mathscr{L}^*_{\mathrm{b},0}$ after adjusting the background contribution $\mathscr{L}^*_{\mathrm{b},0}$. Solid lines refer to the power law $\Delta\mathscr{L}/(k_\mathrm{B}T) \simeq \mathscr{L}_0\tau^{-\nu x_\lambda}$ with $\nu x_\lambda = 0.567$ [Eq. (32)].

data tell that the results for $\mathscr{L}$ as obtained from both methods [Eqs. (26) and (28)] coincide within the error bars. The latter route, however, exhibits superior averaging properties, in line with previous findings for a different system concerning the motion of a tagged particle [73]. The success of the method hinges on evaluating $\delta\mathscr{R}^2_\alpha(t)$ by using a certain "blocking scheme" [46, 50], which resembles a non-averaging multiple-$\tau$ correlator and naturally generates a semi-logarithmic time grid, particularly suitable for the description of slow processes. With this, the time derivative in Eq. (28) can simply be computed from central difference quotients. The results for $\mathscr{L}$ presented here have been obtained by applying this method.

The interdiffusion constant [Eq. (26)] can be decomposed as $D_\mathrm{m} = \Delta D_\mathrm{m} + D_b$ into a singular contribution $\Delta D_\mathrm{m}$ stemming from critical fluctuations in the fluid at large length scales and an omnipresent analytic background term $D_b$ arising due to short-length-scale fluctuations [74]. As predicted by MCT and dynamic RGT, asymptotically close to the critical temperature $\Delta D_\mathrm{m}$ follows the Einstein–Kawasaki relation [17, 75]:

$$\Delta D_\mathrm{m}(T \to T_c) \simeq \frac{R_D k_\mathrm{B}T}{6\pi\bar{\eta}\xi} \simeq D_{m,0}\,\tau^{\nu x_D}, \tag{30}$$

where $R_D$ is a universal dimensionless number which will be discussed in Sec. IV [see Eq. (40) below]; the asymptotic equality on the right defines the critical amplitude $D_{m,0}$ with its dimensionless form $D^*_{m,0} := D_{m,0}\,t_0\sigma^{-2}$. Note that the critical divergences of $\bar{\eta}$ [Eqs. (6) and (7) and $\xi$ imply the power-law singularity of $\Delta D_\mathrm{m}$ [Eq. (30)] and the scaling relation $x_D = 1 + x_\eta$ [see Eqs. (1), (6), and (7)]. It was demonstrated before [38, 41, 42] that the background contribution must be taken into account for a proper description of the simulation data. Anticipating that also the background term is proportional to temperature [43], $D_b(T) = \mathscr{L}_b(T)/\chi(T) \simeq \mathscr{L}_{\mathrm{b},0}k_\mathrm{B}T/\chi(T)$, suggests that the ratio $\mathscr{L}(T)/k_\mathrm{B}T$ is described by the asymptotic law

$$\frac{\mathscr{L}(T)}{k_\mathrm{B}T} \simeq \mathscr{L}_0\tau^{-\nu x_\lambda} + \mathscr{L}_{\mathrm{b},0}\,, \quad T \to T_c\,, \tag{31}$$

with the exponent combination

$$\nu x_\lambda = \nu(1 - \eta - x_\eta) \approx 0.567\,, \tag{32}$$

where we have used Eqs. (1) and (27). The connection to the amplitude of the interdiffusion constant is provided by

$$D_{m,0} = \mathscr{L}_0\,k_\mathrm{B}T_c/\chi_0\,. \tag{33}$$

We have computed $\mathscr{L}$ for five binary liquid mixtures for a wide range of temperatures, $1.01T_c \leqslant T \lesssim 2T_c$ (see Fig. 8; the data for model II are not shown). For the three binary liquid mixtures belonging to model I and within the investigated range of temperatures, $\mathscr{L}/(k_\mathrm{B}T)$ increases by factors between 4.3 and 7.5 upon approaching $T_c$. This indicates the onset of the expected divergence [Eq. (31)]. The remaining task is to determine the values of the critical amplitude $\mathscr{L}_0$ and the background contribution $\mathscr{L}_{\mathrm{b},0}$ for each mixture such that Eq. (31) describes the data. Here, an automated fitting routine is not suitable due to the asymptotic nature of power laws. Instead, the value for $\mathscr{L}_{\mathrm{b},0}$ has been adjusted first, such that plotting $\Delta\mathscr{L}(T)/(k_\mathrm{B}T) := \mathscr{L}(T)/(k_\mathrm{B}T) - \mathscr{L}_{\mathrm{b},0}$ as function of $\tau$ on double-logarithmic scales renders the data to follow straight lines of slope $-\nu x_\lambda$ for intermediate temperatures $0.1 \lesssim \tau \lesssim 0.5$ (Fig. 9). Indeed, subsequently for all investigated mixtures, the critical singularity $\Delta\mathscr{L}(T)/k_\mathrm{B}T \sim \tau^{-\nu x_\lambda}$ [Eq. (31)] can be identified in the data, which allows us to infer the critical amplitudes $\mathscr{L}_0$ (Table I).

However, for small $\tau \lesssim 0.1$, the data for $\Delta\mathscr{L}^*/T^*$ systematically deviate from the asymptotic power law. This is expected due to the emergence of finite-size corrections close to $T_c$ [38, 41, 42], which are significant despite the large simulation boxes used ($L/\xi \gtrsim 7$). We find that $\mathscr{L}_0$ increases by a factor of $\approx 6$ upon decreasing the number density $\varrho$ of the

fluid. On the other hand, the background contribution $\mathscr{L}_{b,0}$ turns out to be almost insensitive to changes in the density so that the background term in Eq. (31) becomes less relevant for smaller $\varrho$.

### 2. *Shear viscosity*

Another transport quantity of central interest is the shear viscosity $\bar{\eta}$ (not to be confused with the critical exponent $\eta$ of the structure factor). Due to critical slowing down, $\bar{\eta}(T)$ is expected to diverge at $T_c$. We have computed this quantity using both the Green–Kubo and the Einstein–Helfand formulae, involving the stress tensor as the generalized current. The Green–Kubo formula reads [68, 76]

$$\bar{\eta} = \frac{\varrho}{3k_{\mathrm{B}}T}\int_0^\infty \Big[C_{xy}(t) + C_{yz}(t) + C_{xz}(t)\Big]\mathrm{d}t \qquad (34)$$

and is based on the autocorrelators $C_{ij}(t)$ of the off-diagonal elements of the stress tensor $\Pi_{ij}$ [Eq. (16)]:

$$C_{ij}(t) = \frac{1}{N}\left\langle \Pi_{ij}(t)\,\Pi_{ij}(0)\right\rangle . \qquad (35)$$

The autocorrelators $C_{ij}(t)$ are normalized by $N$ in order to render a finite value of $C_{ij}(t)$ in the thermodynamic limit.

Starting with the Helfand moments [76, 77]

$$\delta G_{ij}^2(t) = \frac{1}{N}\left\langle \left(\int_0^t \Pi_{ij}(t')\,\mathrm{d}t'\right)^2\right\rangle , \qquad (36)$$

we have computed $\bar{\eta}$ alternatively by means of the Einstein–Helfand formula [76, 77]:

$$\bar{\eta} = \lim_{t\to\infty}\frac{\varrho}{6k_{\mathrm{B}}T}\frac{\mathrm{d}}{\mathrm{d}t}\Big[\delta G_{xy}^2(t) + \delta G_{yz}^2(t) + \delta G_{xz}^2(t)\Big] . \qquad (37)$$

The expressions in Eqs. (35) and (37) explicitly include averages over the different Cartesian directions due to isotropy of the mixed phase. We have checked that both routes yield the same values of $\bar{\eta}$, with the Einstein–Helfand formula generating smaller error bars.

The thermal singularity of $\bar{\eta}$ in model $H'$ is the same as in model $H$ and reads [6, 24]

$$\bar{\eta} \simeq \eta_0 \tau^{-\nu x_\eta} , \qquad \nu x_\eta \approx 0.043 , \qquad (38)$$

which can be expressed as $\bar{\eta} \simeq \eta_0 \xi_0^{-x_\eta}\xi^{x_\eta}$ with $\xi \simeq \xi_0\tau^{-\nu}$ [compare Eq. (6)]. Figure 10 shows the shear viscosity $\bar{\eta}(\tau)$ for three number densities $\varrho$ on double-logarithmic scales. The observed increase of $\bar{\eta}$ by a factor of $\approx 3.3$ as $\varrho\sigma^3$ is varied from 0.7 to 1.0 supports the intuitive picture that transport is slower in denser fluids. In order to facilitate the direct determination of $\eta_0$, instead of performing a finite-size scaling analysis [47], we have considered particularly large system sizes (see the caption of Fig. 10). By fixing the critical exponent to $\nu x_\eta = 0.043$, we have obtained the amplitude $\eta_0$ by fits of Eq. (38) to the data in the temperature range that is unaffected by finite-size effects; the results are listed in Table I. The data for $\bar{\eta}$ at $\varrho\sigma^3 = 1.0$ and 0.8 are compatible with the critical power law (see solid lines in Fig. 10); the divergence, however, is hardly inferred from the figure due to the tiny value of the exponent $\nu x_\eta$, albeit the present error bars for $\bar{\eta}$ are much smaller compared to those reported in the literature. For $\varrho\sigma^3 = 1.0$, due to corrections the data for $\bar{\eta}$ fall short of the asymptotic line for $\tau > 0.2$. For $\varrho\sigma^3 = 0.7$, we refrain from providing a value for $\eta_0$ because for this low density the determination of $\eta_0$ requires enormous statistical averaging, which we have not yet achieved. Yet, from the value $R_D = 1.0$ of the universal amplitude ratio [Eq. (40) below] one finds $\eta_0 \simeq 1.1$. The dashed line in Fig. 10 corresponds to this predicted value.

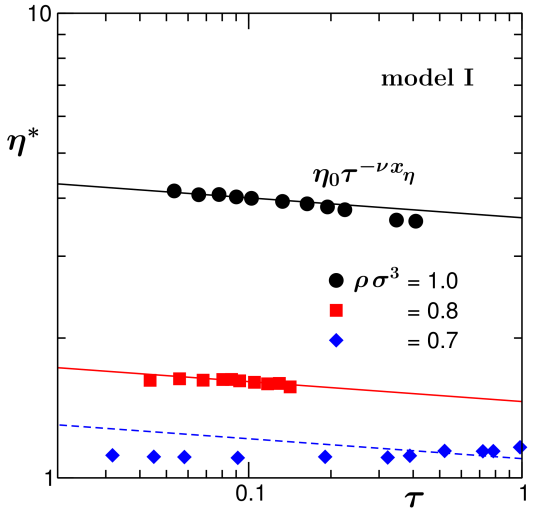


FIG. 10. Dimensionless shear viscosity $\bar{\eta}^* = \bar{\eta}\sigma^3/\varepsilon t_0$ as a function of $\tau$, for model I and three number densities. The chosen system sizes are $L = 47\sigma$, $42\sigma$, and $50\sigma$ for $\varrho\sigma^3 = 1.0$, 0.8, and 0.7, respectively. The straight lines indicate the asymptotic critical exponent $\nu x_\eta \approx 0.043$; solid lines are fits to the data. For $\varrho\sigma^3 = 0.7$, the large error bars have precluded a fit of the amplitude $\eta_0$; instead, $\eta_0$ has been estimated from Eq. (40) using $R_D = 1.0$ (dashed line). Relative errors in $\bar{\eta}$ vary between 2% and 8%. The resulting values of $\eta_0$ are reported in Table I.

Actually, as in the case of the Onsager coefficient $\mathscr{L}$, Eq. (38) has also to be augmented by an analytic background contribution $\eta_b$. For the shear viscosity, this background term has been argued to be of multiplicative character [78], i.e., the universal amplitude $\eta_0$ is proportional to the background viscosity and takes the form $\eta_0 = \eta_b(q_0\xi_0)^{x_\eta}$ with a certain (necessarily system-specific) wavenumber $q_0$ [33, 43]. Thus, in contrast to the case of the Onsager coefficient, the analysis of the critical divergence of the shear viscosity is not hampered by the presence of an analytic background.

## IV. UNIVERSAL AMPLITUDE RATIOS

Generically, critical amplitudes are non-universal and depend on microscopic details of the systems. However, certain ratios of critical amplitudes are known to be universal. One

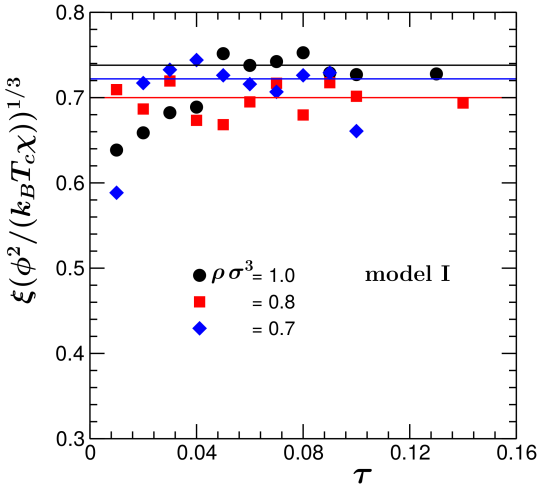


FIG. 11. Temperature dependence of the dimensionless and supposedly universal quantity $\xi(\phi^2/(k_BT_c\chi))^{1/3}$ within model I for three number densities. Symbols correspond to simulation data and solid lines represent averages of the data points.

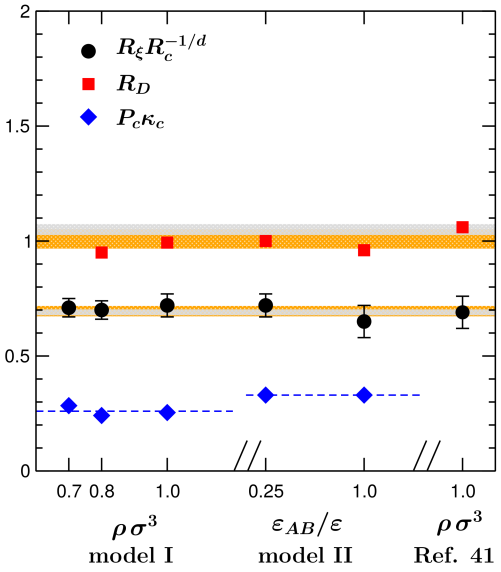


FIG. 12. The universal static amplitude ratio $R_\xi R_c^{-1/d}$, the dynamic universal amplitude ratio $R_D$, and the dimensionless quantity $P_c\kappa_c$ at criticality for various binary liquid mixtures within models I and II. The grey and orange regions represent the ranges of the theoretical and experimental predictions, respectively. The dashed lines correspond to the averages for $P_c\kappa_c$ within models I and II, respectively. The relative error bars of $R_D$ are about 20%.

such ratio for static quantities is [4, 5, 79]

$$R_\xi^+ R_c^{-1/d} = \xi_0^+ \left( \frac{\varphi_0^2}{k_B T_c \chi_0^+} \right)^{1/d} , \qquad (39)$$

as predicted by the hypothesis of two-scale factor universality. Here, the superscript "+" emphasizes that (apart from $\varphi_0$) the amplitudes correspond to $T > T_c$. For binary liquid mixtures belonging to the 3d Ising universality class, the value of $R_\xi^+ R_c^{-1/d}$, as estimated theoretically and experimentally, lies within the ranges [0.68, 0.70] and [0.67, 0.72], respectively [5].

The so-called Kawasaki amplitude $R_D = 6\pi\bar{\eta}\xi/(k_B T \Delta D_m)$ [Eq. (30)] is a universal amplitude ratio involving transport coefficients, i.e., the critical enhancement $\Delta D_m$ of the mutual diffusivity [Eq. (30)]. Inserting the asymptotic singular behaviors of $\xi$, $\chi$, and $\bar{\eta}$ [Eqs. (24) and (38)] as well as $\Delta D_m \simeq \mathscr{L}_0 \tau^{-\nu x_\lambda}/\chi_0$ [see Eqs. (27) and (31)], the temperature dependence drops out and one finds

$$R_D = \frac{6\pi\eta_0\xi_0\mathscr{L}_0}{\chi_0} . \qquad (40)$$

This combination of non-universal static and dynamic critical amplitudes has been shown to be a universal number [74]. Theoretical calculations based on dynamic RGT predict $R_D \approx 1.07$ [25], while MCT provides $R_D \approx 1.03$ [33]; experimental data yield $R_D = 1.01 \pm 0.04$ [33, 74].

A calculation of the amplitude ratio $R_\xi^+ R_c^{-1/d}$ in Eq. (39) combines the uncertainties in the separately determined amplitudes $\varphi_0$, $\xi_0$, and $\chi_0$. Table I lists these values. Equivalently, the universal ratio is given directly as the limit $\tau \searrow 0$ of the combination $Z(\tau) := \xi(\tau)[\phi(\tau)^2/(k_B T_c \chi(\tau))]^{1/3}$. However, the omnipresent finite-size corrections prohibit us from taking the limit rigorously. Yet, one can expect to find a temperature range close to $T_c$ in which all quantities $\phi$, $\xi$, and $\chi$ follow their asymptotic critical laws. This implies that in this temperature range $Z(\tau)$ displays a plateau at the value of $R_\xi^+ R_c^{-1/d}$. Figure 11 provides a test of this approach for the three mixtures within model I. Indeed, a plateau may be inferred for each data set after averaging out the scatter of the data points. The estimates of $R_\xi^+ R_c^{-1/d}$ obtained this way (0.738 ± 0.016, 0.70 ± 0.03, 0.722 ± 0.023 for $\varrho\sigma^3 = 1.0$, 0.8, 0.7, respectively, within model I) match well with those obtained from Eq. (39) by inserting the critical amplitudes, but exhibit slightly smaller errors. The results for the 5 binary mixtures studied here as well as the results of Ref. [42] corroborate that $R_\xi^+ R_c^{-1/d}$ is a universal number with a value of 0.70 ± 0.01 (Fig. 12). Our estimate for $R_\xi^+ R_c^{-1/d}$ is in nice agreement with previous values for this universal ratio obtained from theory and experiments [see text below Eq. (39)].

Concerning the dynamic amplitude ratio $R_D$, we report results for model I only for $\varrho\sigma^3 = 1.0$ and 0.8 because it is difficult to resolve the critical behavior of the viscosity at low densities. A similar analysis as above in terms of $Y(\tau) = 6\pi\eta\xi\Delta\mathscr{L}/k_B T\chi$ has turned out to be inconclusive, in that no plateau in $Y(\tau)$ has emerged. We attribute this to the fact that the critical range of temperatures (free from both asymptotic and finite-size corrections) for the Onsager coefficient is located at higher temperatures than for the other quantities entering Eq. (40) (see also Figs. 6, 7, 9, and 10). Therefore, Table I lists the values for $R_D$ as obtained from Eq. (40). Despite significant error bars of about 20%, the estimates coincide surprisingly well with the expectation $R_D \approx 1.0$ (Fig. 12)

Finally, we note that the dimensionless product $P_c\kappa_c$ of pres-

sure and compressibility at the demixing transition appears to stay almost constant at $0.26 \pm 0.02$ within model I (insensitive to the density $\varrho$) and at ca. 0.33 for model II (insensitive to the strength $\epsilon_{\mathrm{AB}}$ of repulsion). This is remarkable because $P_c$ and $\kappa_c$ separately vary across these ranges by almost an order of magnitude. However, here we point out that the product $P_c\kappa_c$ is not related to the order parameter field, which is the concentration, but to the number density field, which in model $H'$ serves as a secondary conserved field [6]. Thus, there is no theoretical basis to consider $P_c\kappa_c$ as a universal number; indeed the values of $P_c\kappa_c$ are different for models I and II.

## V. SUMMARY AND CONCLUSIONS

We have computationally investigated the static and dynamic properties of five symmetric binary liquid mixtures close to their continuous demixing transitions. To this end, we have employed a combination of Monte Carlo simulations in the semi-grand canonical ensemble and molecular dynamics (MD) simulations. While the former is suited best to determine the phase diagram, only the latter obeys the conservation laws of actual liquid mixtures and thus properly captures the critical dynamics associated with model $H'$. Previous computational studies of the critical behavior of such mixtures have been based on small system sizes in conjunction with suitable finite-size scaling analyses. A massively parallel implementation of the MD simulations using GPUs made it possible to explore much larger system sizes than before, which has allowed us to determine the critical amplitudes directly.

The chosen mixtures represent a wide range of critical temperatures $T_c$, number densities $\varrho$, and isothermal compressibilities $\kappa_T$. For all mixtures considered, the particles interact via truncated Lennard-Jones potentials. The interaction potential $u_{\mathrm{AB}}(r)$ for pairs of unlike particles has been chosen to either include the usual attractive part or to be purely repulsive, which we refer to as models I and II, respectively. For the fluids in model I, the density $\varrho$ has been varied, while within model II the strength $\varepsilon_{\mathrm{AB}}$ of the repulsion between unlike species has been varied. All results of the data analysis have been compiled in Table I. The main findings of our work are the following:

*(i)* For each fluid, we have calculated the phase diagram in the temperature–composition plane, from which the corresponding critical temperatures $T_c$ have been extracted by using the critical scaling of the order parameter (Fig. 1) and Binder's intersection method (Fig. 2). We have found that the values of $T_c$ within model II are a factor of ca. 2 higher than for otherwise comparable fluids in model I. Within model II, reinforcing the repulsion $\varepsilon_{AB}$ leads to a drastic increase of $T_c$. Further, at the demixing transition, we have computed the pressure $P_c$ and the isothermal compressibility $\kappa_c$, which exhibit a large variability across all mixtures, covering almost one order of magnitude.

*(ii)* The loci of the liquid–liquid critical points $T_c(\varrho)$, also referred to as $\lambda$-line, has been calculated within model I. This curve $T_c(\varrho)$ is non-monotonic, indicating a re-entrance phenomenon upon varying the density along an isotherm (Fig. 3). In this context, for model I we have also investigated the potential occurrence of a critical end point or a tri-critical point at which the $\lambda$-line meets the liquid–vapor critical point. Our results for the isothermal compressibility (Fig. 5) indicate at that this is not the case. This issue calls for additional future investigations.

*(iii)* The structural properties of the mixtures have been analyzed in terms of the static structure factors $S_{cc}(k)$ and $S_{\varrho\varrho}(k)$ of the composition and density fields, respectively (Fig. 4). As expected, long-wavelength fluctuations of the composition become dominant near the demixing transition: for small wave numbers, $S_{cc}(k \to 0)$ increases sharply as $T_c$ is approached, at which the critical power law $S_{cc}(k) \sim k^{-2+\eta}$ is observed over one decade in $k$ which is facilitated by the large system sizes chosen. To the contrary, $S_{\varrho\varrho}(k)$, which is probing density fluctuations, is almost insensitive to temperature changes in the range $T_c \leqslant T < 1.6T_c$; in particular, it does not display any critical enhancement at small $k$.

*(iv)* From $S_{cc}(k)$ we have determined the correlation length $\xi$ and the order parameter susceptibility $\chi$. For both quantities, the scaling with the corresponding critical Ising exponents is confirmed (Figs. 6 and 7), allowing us to extract the non-universal critical amplitudes $\xi_0$ and $\chi_0$. We have found that $\chi_0$ decreases upon increasing density (model I), which we attribute to an energetically penalized particle rearrangement at denser packing. The values of $\chi_0$ are less sensitive to changes in the strength of the AB repulsion (model II). The correlation length $\xi$ is limited by the finite system size. Nonetheless we have been able to achieve values of up to $\xi \approx 10\sigma$ in our simulations. Across all five binary fluid mixtures, its amplitude varies only mildly around $\xi_0 \approx 0.5\sigma$.

*(v)* The critical transport behavior has been studied in terms of the Onsager coefficient $\mathscr{L} = \chi D_m$ and the shear viscosity $\bar{\eta}$, the former also determining the interdiffusion constant $D_m$. Within model I, the Onsager coefficient and thus its critical amplitude $\mathscr{L}_0$ increase by a factor of 6 upon varying the density from $\varrho\sigma^3 = 1$ to 0.7 (Figs. 8 and 9); concomitantly, the shear viscosity $\bar{\eta}$ decreases by a factor of 3 (Fig. 10). This trend is in line with our notion that mass diffusion is faster in a less dense fluid; it also has direct consequences for the computational efficiency of a model. The asymptotic critical enhancement of $\mathscr{L}$ is obscured, first, by the non-universal analytic background contribution away from $T_c$ and, second, by finite-size corrections close to $T_c$, which are still significant despite the large simulation boxes we used. These issues have prevented us to obtain accurate estimates of $\mathscr{L}_0$. Furthermore, the critical behavior of $\bar{\eta} \sim |T - T_c|^{-\nu x_\eta}$, $\nu x_\eta \approx 0.043$, is difficult to assess reliably due to the smallness of the critical exponent. We have obtained the critical amplitude for 3 out of the 5 mixtures (within model I for $\varrho\sigma^3 = 1$, 0.8 and within model II for $\epsilon_{AB} = 0.25\varepsilon$).

*(vi)* Finally, we have computed two universal amplitude ratios, involving several static and dynamic non-universal critical amplitudes (all above $T_c$). One such ratio of static quantities is $R_\xi^+ R_c^{-1/3}$ [Eq. (39)], the other ratio $R_D$ is a combination of both static and dynamic amplitudes [Eq. (40)]. For both ratios, quantitative predictions are available for the universality classes of the models $H$ and $H'$ based on mode-coupling and dynamic renormalization group theories, which are supported by experi-

mental data. Across all 5 mixtures studied and including the results of Ref. [42], the simulation results for the static ratio $R_\xi^+ R_c^{-1/3}$ yield a universal value $0.70 \pm 0.01$, in agreement with theoretical predictions (Fig. 12). Our results for the dynamic ratio $R_D$ are compatible with theoretical and experimental estimates, but they are subject to large uncertainties given the difficulties in determining the dynamic critical amplitudes $\mathscr{L}_0$ and $\eta_0$. A notable finding is that the dimensionless product $P_c\kappa_c$ of pressure and compressibility is remarkably constant along the $\lambda$-line in model I and with respect to variations of the strength $\varepsilon_{\mathrm{AB}}$ of repulsion in model II (Fig. 12).

The present study reports the first comprehensive analysis of the density dependence of the critical amplitudes. The knowledge of these amplitudes for a given simulation model facilitates the calibration of the model to a given physical binary liquid mixture. As an example we refer to the well-characterized water–lutidine mixture [80] and model I for $\varrho\sigma^3 = 0.7$: first, the measured correlation length amplitude $\xi_0 \approx 0.2\,\mathrm{nm}$ implies the length scale $\sigma \approx 0.4\,\mathrm{nm}$ for all of the presented simulations. Second, the relaxation rate amplitude $\Gamma_0 \approx 25 \times 10^9\,\mathrm{s}^{-1}$ yields the critical amplitude of the interdiffusion constant $D_{m,0} = \Gamma_0\xi_0^2/2 \approx 5 \times 10^{-10}\,\mathrm{m}^2\,\mathrm{s}^{-1}$, which has to be compared with the simulation result $D_{m,0} \approx 0.09\sigma^2/t_0$, fixing the time scale $t_0 \approx 30\,\mathrm{ps}$. The energy scale $\varepsilon$ is set by the critical temperature, $T_c \approx 307\,\mathrm{K}$ in the experiments and $k_\mathrm{B}T_c \approx 1.51\varepsilon$ in the simulations, and thus $\varepsilon/k_\mathrm{B} \approx 203\,\mathrm{K}$ or $\varepsilon \approx 2.8 \times 10^{-21}\,\mathrm{J}$. Accordingly, the universal amplitude ratios fix the critical amplitudes for a number of related physical quantities such as the composition susceptibility $\chi_0$, the viscosity $\eta_0$, or the surface tension [81]. The coarse-grained simulation models (replacing an organic molecule and water by symmetric Lennard-Jones spheres), however, come at the price that physical quantities not linked to the critical singularities may not be captured correctly. For instance, along these lines, the pressure at criticality is expected to be $P_c \approx 110\,\mathrm{MPa}$, which is 3 orders of magnitude larger than the ambient pressure, while the compressibility $\kappa_c \approx 25 \times 10^{-10}\,\mathrm{Pa}^{-1}$ is too high as well. Increasing the density $\varrho$ will reduce the compressibility, but simultaneously increase the pressure and also slow down the overall dynamics (which is computationally expensive). Quantitative agreement with actual binary liquid mixtures can be achieved with force-field-based simulation models, see [82] for a recent study. Nevertheless, the comparably simple models discussed here can correctly describe the physical behavior at long wave length thanks to the universality of the demixing transition. The presented compilation of results may serve as a guide to find the simulation model that is best suited to address a specific phenomenon.

This study is supposed to stimulate further computational investigations concerning critical transport in fluids. Specifically, so far there are no dedicated computations of dynamic critical amplitudes *below* $T_c$ and also none for liquid–vapor transitions, neither above nor below $T_c$. A quantitatively reliable determination of the ratio $\eta_0/\eta_b$ is also of significant importance, in particular in view of the difficulties associated with obtaining an accurate value of this ratio from experiments.

## ACKNOWLEDGMENTS

We acknowledge the use of the supercomputer *Hydra* of the Max Planck Computing and Data Facility Garching for producing most of the MD data.

[1] M. E. Fisher, Rep. Prog. Phys. **30**, 615 (1967).
[2] H. Stanley, *Introduction to Phase Transitions and Critical Phenomena* (Oxford University Press, Oxford, 1971).
[3] P. C. Hohenberg and B. I. Halperin, Rev. Mod. Phys. **49**, 435 (1977).
[4] V. Privman, P. Hohenberg, and A. Aharony, in *Phase Transitions and Critical Phenomena*, Vol. 14, edited by C. Domb and J. Lebowitz (Academic, New York, 1991) Chap. 1, pp. 1–134.
[5] A. Pelissetto and E. Vicardi, Phys. Rep. **368**, 549 (2002).
[6] R. Folk and G. Moser, J. Phys. A **39**, R207 (2006).
[7] M. E. Fisher, Rev. Mod. Phys. **70**, 653 (1998).
[8] P. Heller, Rep. Prog. Phys. **30**, 731 (1967).
[9] J. V. Sengers and J. G. Shanks, J. Stat. Phys. **137**, 857 (2009).
[10] C. Hertlein, L. Helden, A. Gambassi, S. Dietrich, and C. Bechinger, Nature **451**, 172 (2008).
[11] I. Buttinoni, G. Volpe, F. Kümmel, G. Volpe, and C. Bechinger, J. Phys: Condens. Matter **24**, 284129 (2012).
[12] M. Anisimov and J. Sengers, in *Equations of State for Fluids and Fluid Mixtures*, Experimental Thermodynamics V, edited by J. Sengers, R. Kayser, C. Peters, and H. White (Elsevier, Amsterdam, 2000) Chap. 11, pp. 381–434.
[13] K. Binder, Mol. Phys. **108**, 1797 (2010).
[14] K. Binder, Z. Phys. B **43**, 119 (1981).
[15] D. Landau and K. Binder, *A Guide to Monte Carlo Simulations in Statistical Physics*, 3rd ed. (Cambridge University Press, Cambridge, 2009).
[16] N. B. Wilding and P. Nielaba, Phys. Rev. E **53**, 926 (1996).
[17] A. Onuki, Phys. Rev. E **55**, 403 (1997).
[18] J. K. Bhattacharjee, U. Kaatze, and S. Z. Mirzaev, Rep. Prog. Phys. **73**, 066601 (2010).
[19] A. Furukawa, A. Gambassi, S. Dietrich, and H. Tanaka, Phys. Rev. Lett. **111**, 055701 (2013).
[20] A. Onuki, *Phase Transition Dynamics* (Cambridge University Press, Cambridge, 2002).
[21] R. Folk and G. Moser, Int. J. Thermophys. **16**, 1363 (1995); Phys. Rev. Lett. **75**, 2706 (1995).
[22] L. P. Filippov, Int. J. Heat Mass Transfer **11**, 331 (1968).
[23] H. Hao, R. A. Ferrell, and J. K. Bhattacharjee, Phys. Rev. E **71**, 021201 (2005).
[24] J. K. Bhattacharjee and R. A. Ferrell, Phys. Lett. A **88**, 77 (1982).
[25] G. Paladin and L. Peliti, J. Physique Lett. **43**, 15 (1982).
[26] B. I. Halperin, P. C. Hohenberg, and E. D. Siggia, Phys. Rev. B **13**, 1299 (1976).
[27] R. F. Berg, M. R. Moldover, and G. A. Zimmerli, Phys. Rev. E **60**, 4079 (1999).
[28] M. E. Fisher, Phys. Rev. **176**, 257 (1968).
[29] T. Ohta and K. Kawasaki, Prog. Theor. Phys. **55**, 1384 (1975).
[30] L. P. Kadanoff and J. Swift, Phys. Rev. **166**, 89 (1968).
[31] K. G. Wilson and M. E. Fisher, Phys. Rev. Lett. **28**, 240 (1972).

[32] R. Bausch, H. K. Janssen, and H. Wagner, Z. Phys. B **24**, 113 (1976).
[33] H. C. Burstyn, J. V. Sengers, J. K. Bhattacharjee, and R. A. Ferrell, Phys. Rev. A **28**, 1567 (1983).
[34] J. Swift, Phys. Rev. **173**, 257 (1968).
[35] K. A. Gillis, I. I. Shinder, and M. R. Moldover, Phys. Rev. E **72**, 051201 (2005).
[36] K. Jagannathan and A. Yethiraj, Phys. Rev. Lett. **93**, 015701 (2004).
[37] A. Chen, E. H. Chimowitz, S. De, and Y. Shapir, Phys. Rev. Lett. **95**, 255701 (2005).
[38] S. Roy and S. K. Das, EPL (Europhys. Lett.) **94**, 36001 (2011).
[39] K. Meier, A. Laesecke, and S. Kabelac, J. Chem. Phys. **122**, 014513 (2005).
[40] K. M. Dyer, B. M. Pettitt, and G. Stell, J. Chem. Phys. **126**, 034502 (2007).
[41] S. K. Das, M. E. Fisher, J. V. Sengers, J. Horbach, and K. Binder, Phys. Rev. Lett. **97**, 025702 (2006).
[42] S. K. Das, J. Horbach, K. Binder, M. E. Fisher, and J. V. Sengers, J. Chem. Phys. **125**, 024506 (2006).
[43] S. K. Das, J. V. Sengers, and M. E. Fisher, J. Chem. Phys. **127**, 144506 (2007).
[44] M. Fisher, in *Critical Phenomena*, Proc. Enrico Fermi Int. School of Physics, Vol. 51, edited by M. Green (Academic, New York, 1971) pp. 1–99.
[45] S. Roy and S. K. Das, J. Chem. Phys. **139**, 064505 (2013).
[46] D. Frenkel and B. Smit, *Understanding Molecular Simulations: From Algorithm to Applications* (Academic, San Diego, 2002).
[47] S. Roy and S. K. Das, J. Chem. Phys. **141**, 234502 (2014).
[48] T. Voigtmann and J. Horbach, Phys. Rev. Lett. **103**, 205901 (2009).
[49] J. Zausch, J. Horbach, P. Virnau, and K. Binder, J. Phys.: Condens. Matter **22**, 104120 (2010).
[50] P. H. Colberg and F. Höfling, Comput. Phys. Commun. **182**, 1120 (2011).
[51] J. D. Weeks, D. Chandler, and H. C. Andersen, J. Chem. Phys. **54**, 5237 (1971).
[52] B. Widom and J. S. Rowlinson, J. Chem. Phys. **52**, 1670 (1970).
[53] U. Täuber, *Critical Dynamics: A Field Theory Approach to Equilibrium and Non-Equilibrium Scaling Behavior* (Cambridge University Press, London, 2014).
[54] M. Allen and D. Tildesley, *Computer Simulations of Liquids* (Clarendon, Oxford, 1987).
[55] J. A. Baker and J. D. Hirst, Mol. Inform. **30**, 498 (2011).
[56] M. Weigel, A. Arnold, and P. Virnau, Eur. Phys. J. Special Topics **210**, 1 (2012).
[57] "Highly Accelerated Large-scale Molecular Dynamics package," (2007–2016), version 1.0, see `http://halmd.org`.
[58] A. P. Ruymgaart, A. E. Cardenas, and R. Elber, J. Chem. Theory Comput. **7**, 3072 (2011).
[59] P. de Buyl, P. Colberg, and F. Höfling, Comput. Phys. Commun. **185**, 1546 (2014).
[60] F. Höfling and S. Dietrich, EPL (Europhys. Lett.) **109**, 46002 (2015).
[61] G. J. Martyna, M. L. Klein, and M. Tuckerman, J. Chem. Phys. **97**, 2635 (1992).
[62] S. K. Das, J. Horbach, and K. Binder, J. Chem. Phys. **119**, 1547 (2003).
[63] S. Toxvaerd and E. Velasco, Mol. Phys. **86**, 845 (1995).
[64] N. B. Wilding, Phys. Rev. E **55**, 6624 (1997).
[65] S. Dietrich and A. Latz, Phys. Rev. B **40**, 9204 (1989).
[66] T. Getta and S. Dietrich, Phys. Rev. E **47**, 1856 (1993).
[67] S. Dietrich and M. Schick, Surf. Sci. **382**, 178 (1997).
[68] J.-P. Hansen and I. McDonald, *Theory of Simple Liquids* (Academic, London, 2008).
[69] A. B. Bhatia and D. E. Thronton, Phys. Rev. B **2**, 8 (1970).
[70] Y. Zhou and G. H. Miller, J. Phys. Chem. **100**, 5516 (1996).
[71] J. Horbach, S. K. Das, A. Griesche, M.-P. Macht, G. Frohberg, and A. Meyer, Phys. Rev. B **75**, 174304 (2007).
[72] N. Höft, *Diffusion dynamics in two-dimensional fluids*, Master Thesis, Universität Düsseldorf, Germany (2012).
[73] F. Höfling and T. Franosch, Phys. Rev. Lett. **98**, 140601 (2007).
[74] J. Sengers, Int. J. Thermophys. **6**, 203 (1985).
[75] K. Kawasaki and S.-M. Lo, Phys. Rev. Lett. **29**, 48 (1972).
[76] B. J. Alder, D. M. Gass, and T. E. Wainwright, J. Chem. Phys. **53**, 3813 (1970).
[77] S. Viscardy and P. Gaspard, Phys. Rev. E **68**, 041204 (2003).
[78] T. Ohta, J. Phys. C **10**, 791 (1977).
[79] D. T. Jacobs, Phys. Rev. A **33**, 2605 (1986).
[80] S. Mirzaev, I. Iwanowski, M. Zaitdinov, and U. Kaatze, Chem. Phys. Lett. **431**, 308 (2006).
[81] S. K. Das and K. Binder, Phys. Rev. Lett. **107**, 235702 (2011).
[82] G. Guevara-Carrion, T. Janzen, Y. M. Munoz-Munoz, and J. Vrabec, J. Chem. Phys. **144**, 124501 (2016).